Current Science
CS 5 (3), 2771-2792 (2025)
Received 09 March 2025 | **Revised 15 April** 2025 | **Accepted 10 May**. 2025 | **Online Available 03 June** 2025
https://doi.org/ 10.52845/CS/2025-5-3-56

Current Science

Current Science

OPEN ACCESS

ISSN(O)2795-8639

Original Article

Research on the Mechanical Behavior of CFRP Dovetail Structure under the Bending Action of Airdrop Equipment for the Improvement of Comprehensive Support Efficiency

Yujian Han[a], Yabin Wang[a*], Shuai Yue[a*], Yu Zhang[a], Hongli Jia[a], Xianming Shi[a], Bin Liu[a], Shiqi Li[a]

[a]Shijiazhuang Campus, Army Engineering University,050003 Shijiazhuang, China

[*]Corresponding Author: Yabin Wang, Shuai Yue

Abstract:

Summary: Equipment support is the premise and foundation for maintaining and strengthening emergency rescue capabilities. Under the background of informatization and intelligence, airdrop has become a means of efficient equipment supply support coupled with new styles such as coupling joint emergency rescue and distributed support. Considering the comprehensive support requirements of equipment, strengthening the support design of airdrop equipment, planning and developing support resources. This paper focuses on the mechanical behavior of CFRP dovetail structure under the bending action of airdrop equipment, explores the tensile properties of the structure, and designs and manufactures three carbon fiber dovetail structures with different tenon numbers. Four-point bending and three-point bending tests are performed. Combined with the DIC strain test system, the mechanical properties and failure modes of the structure under bending were analyzed, and a finite element progressive damage model was established based on the LaRC05 criterion to analyze the influence of the interlayer bond strength of carbon fiber and different ply angles on its bending performance, so as to provide reference for effectively improving the comprehensive support efficiency of airdrop equipment.

Keywords: Equipment Support, Bending Action, CFRP Dovetail Tenon, Mechanical Behavior

1. Introduction

To a certain extent, rescue depends on support, and stable and reliable equipment support is the source of the rescue team's ability to perform tasks for a long time. In the new era, the characteristics of three-dimensional deployment, precise implementation, and multi-domain alliance of equipment support are becoming more and more obvious, and the requirements for the overall comprehensive integration of various elements are getting higher and higher. In modern emergency rescue, the airdrop equipment quickly forms a support force and maintains the combat effectiveness of the team, but the structure of the airdrop equipment support materials has a very prominent impact on the comprehensive support efficiency. The effectiveness of equipment support resources does not exist in isolation, but is deeply reflected in every link of equipment development. From the initial design concept, to the selection and application of materials, to the fine polishing of the production process, every step of the decision is directly related to the performance of the equipment on the future battlefield and the difficulty of its support. Therefore, in the early stage of equipment development, it is necessary to take into account the support factors to ensure that the equipment is easy to maintain and repair while having excellent performance, so as to build a set of efficient and flexible support system.

Among the various types of airdrop equipment support components, the mortise and tenon structure in traditional carpentry techniques has high research value, and this technique of achieving a stable connection without nails or glue shows the subtlety of material structure

design. When the mortise and tenon structure is skillfully applied to modern military equipment, its characteristics of easy disassembly and convenient maintenance have been vividly brought into play. When the equipment suffers damage, especially to a large extent, the parts with mortise and tenon structure can be replaced or repaired quickly and accurately, which greatly shortens the maintenance cycle of the equipment and improves the overall support efficiency. More importantly, the application of mortise and tenon structure reflects a change in the concept of equipment support—from passive response to injury to active prevention and maintenance. By designing a structure that is easy to disassemble and maintain, equipment users and maintenance personnel can more intuitively understand the status of the equipment, find and deal with potential problems in time, thus effectively avoiding major failures caused by the accumulation of small problems and ensuring the continuous performance of the equipment.

In this paper, we focus on the mechanical behavior of material structures around the airdrop equipment support of mortise and tenon joints, and carbon fiber, as a composite material with excellent mechanical properties, has been widely used in aerospace, marine, vehicles, and construction fields [1-4]. In the production of carbon fiber structure, the method of molding can reduce the generation of cracks, to ensure that it has excellent strength, but it is necessary to make the corresponding metal mold, in the face of large and medium-sized complex structures, the processing difficulty of the mold increases so that the production time and cost are significantly increased, so the researchers assemble and form the simple carbon fiber structure by making a simple carbon fiber structural part by connecting.

At present, the main connection methods of carbon fiber are mechanical connection and glue connection, of which mechanical connection is divided into bolt and rivet connection. According to the existing literature [5-7], bolted joints have attracted a lot of attention from scholars because of their high strength, stability and reliable connection performance. For example, Scattina et al. [8] bolted the composite material and the aluminum plate, and found that creep tends to cause a significant reduction in the bolted joint performance. Liu et al. [9] investigated the effects of bolted joints of different sizes on the bearing performance of carbon fiber plates, and finally established a model for predicting the dimensional strength of bolted holes based on the Weibull distribution theory. Although rivet connections are less reliable than bolted joints in mechanical connections, rivet connections are more suitable in some specific occasions, such as aircraft structural parts that do not need to be disassembled frequently, and the connection of specific structures on automated lines for rapid production [10-12]. The advantages of adhesive joints over mechanical connections are that they can avoid the stress concentration problems in bolted joints and do not consider electrochemical corrosion, so the research on adhesive joints has also attracted the attention of some scholars [13-16], and Çalık et al. [17] have carried out research on single lap joints in adhesive joints, using fiber fabrics and aluminum alloys as bonding materials, and found that carbon fiber fabrics can significantly improve the bonding performance compared with other fiber fabrics through tensile tests. Ashong et al. [18] investigated the effect of hydrofluoric acid on the interface bonding properties of aluminum alloys with carbon fibers, and found that the formation of MgO and C-F chemical bonds is essential for joint strength. Sun et al. [19] used a new suture joint to increase the joint strength of carbon fiber glue joints, and the test results showed that suture joints can effectively improve the tensile strength of single lap and double lap joints. Whitehouse et al. [20] developed a novel profile concept that effectively improves the mechanical properties of the bonded joints between metal adherents and composite substrates.

At present, mechanical and glued joints are still the mainstream of carbon fiber connections, but their application in carbon fiber structures still faces many difficulties, such as aerospace, construction, military fields, in the face of irregular and complex large and medium-sized structures, the above connections are faced with difficult design and complex manufacturing processes, high cost and other problems. Therefore, it is of great significance to propose a carbon fiber connection method that can adapt to different complex situations. After consulting a large number of documents [21-24], a kind of connection structure with good connection stability, durability and seismic performance was

found from ancient Chinese buildings-mortise and tenon structure, which is not only varied, but also basically used in large-scale buildings, so scholars have begun to deepen its research, Chen et al. [25] have studied the mechanical properties of the ring head mortise and tenon joint. Through the experiment, it can be seen that when the width of the tenon is 0.4D, the horizontal splitting failure occurs on the outside of the tenon except for the tensile failure on the top or bottom surface of the tenon on the plane node and the space node. Zhang et al. [26] explored the influence of different inclination angles on the joint performance of mortise and tenon structures, and according to the test results, it can be seen that the larger the inclined rotation, the smaller the size of the hysteresis loop of the inclined joint, and the more obvious the initial negative slip and pinching effect, which leads to the degradation of the ultimate bending moment, initial elastic stiffness and ductility of the specimen. Lu et al. [27] studied the effects of different environmental humidity on the joint performance of mortise and tenon structures, and found that the rotational stiffness of the tenon was significantly reduced in the humid environment, resulting in an increase in the gap at the mortise and tenon joints and a decrease in durability.

For a long time, the mortise and tenon structure has been basically used in wood, and as its excellent properties are gradually known, it has begun to appear in many materials, and carbon fiber composites have similar anisotropic characteristics with wood [28-29], so there is reason to believe that the mortise and tenon structure can also be applied to carbon fiber composites, which not only provides a new research direction for the connection mode of carbon fiber. Qin et al. [30] designed a carbon fiber dovetail structure and conducted a tensile test on it, and found that the structure has good tensile performance and good designability, Aqel et al. [31] tried to use the dovetail structure as the connecting node of the composite sandwich, and carried out bending experiments on it, and established a parametric finite element model. It is found that the ultimate strength of the composite sandwich with dovetail characteristics is greatly improved.

2 CFRP Dovetail Joint Bending Test

2.1 Specimen Making

As shown in Fig. 1(a), T300 carbon fiber unidirectional prepreg cloth of 0° and 90° is produced by prepreg material, respectively. The prepreg cloth is placed in the hot press according to the layup sequence of $[0°/90°]_{25}$. The carbon fiber sheet is produced after being kept at a temperature of 120 °C and a pressure of 0.1MPa for 12h. Then the three-axis CNC machine tool (model CNC-850) is used to cut it, as shown in Figure 1-1(b), where ① and ② are called male and female tenon respectively, and the male and tenon are inserted into the female tenon slot to obtain the CFRP dovetail tenon structure, whose total length (L) is 208±1mm, and width (w) is 45±0.2mm. The thickness (T) is 10±0.1mm. A total of three kinds of specimens were produced. The schematic diagram of the size marks of the tenon is shown in Fig. 1(c), and the specific size parameters are shown in Table 1.

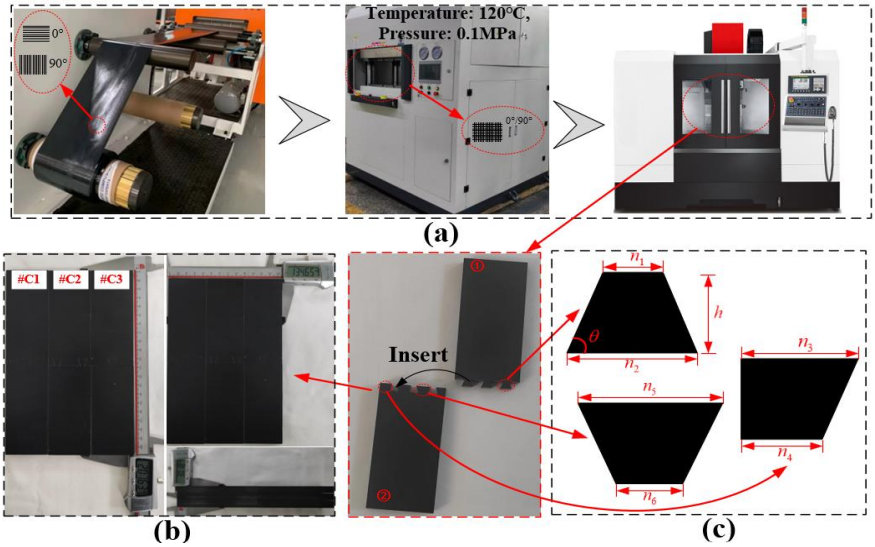

Figure 1 CFRP dovetail structure (a) Production process (b) Three different specimen sizes (c) tenon

parameters

Table 1 Specimen sizes

ID	θ	n_1/mm	n_2/mm	n_3/mm	n_4/mm	n_5/mm	n_6/mm	h/mm
C1	71°	4	9.51	6	3.25	10.5	4.99	8
C2	71°	4	9.51	6	3.25	25	19.49	8
C3	71°	4	9.51	20.5	17.75			8

2.2 Four-Point Bending Test

As shown in Fig. 2, four-point bending test of the CFRP dovetail specimen was carried out using an Instron 5982 material testing machine according to ASTM D7264 test standard. There is only pure bending between the two indenters. The indenter is made of No. 45 steel. The radius (R) is 3mm. The span (L_A) of the support is 160mm. The relationship between the two indenters' distance and the support's span in the four-point bending test is $L_A/2$, and is placed symmetrically. Head drop rate is set to 2mm/min. The strain condition of the specimen during bending was obtained and tested by the digital speckle method (DIC). Make the speckle pattern first： Brush the surface of the specimen with white paint and spray with black spots. Then an industrial camera (Filier, GS3-PGE60SM-C) was used to set up automatic shooting at a rate of 1 frame/SEC to capture the entire test process.

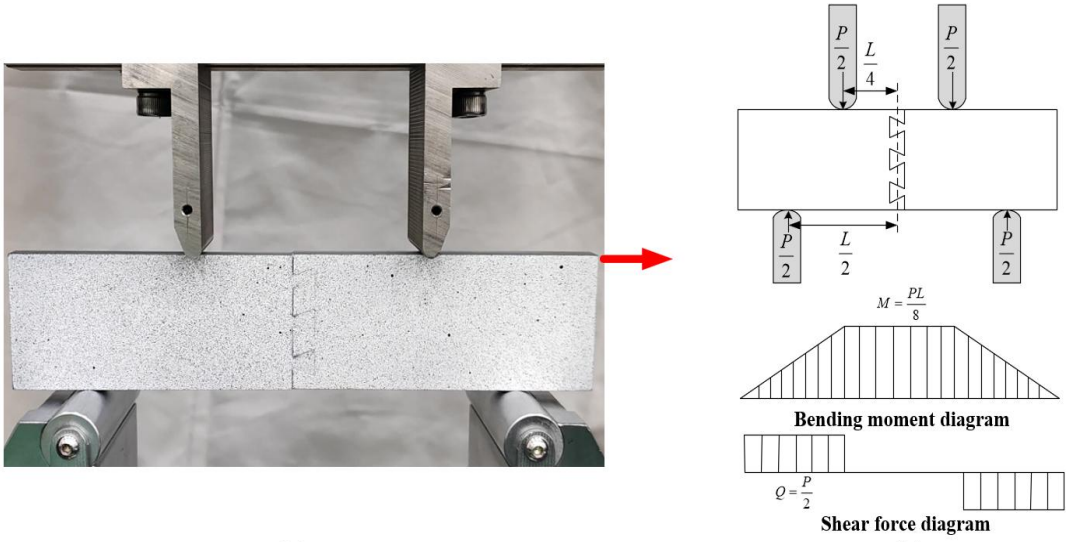

Figure 2 Test setup (a) four-point bending test diagram (b) bending moment diagram and shear diagram

2.3 Three-Point Bending Test

Based on the four-point bending test, the failure mechanism of the CFRP dovetail structure under the action of non-pure bending was studied through a three-point bending test. As shown in Fig. 3(a), the indenter with radius (R) of 3mm is placed at the center of the specimen. According to the shear diagram and bending moment diagram shown in Fig. 3(b), it can be determined that the tenon has not only bending but also shearing action. Other boundary conditions are the same as four-point bending, and DIC tests are also used to analyze the strain throughout the test process.

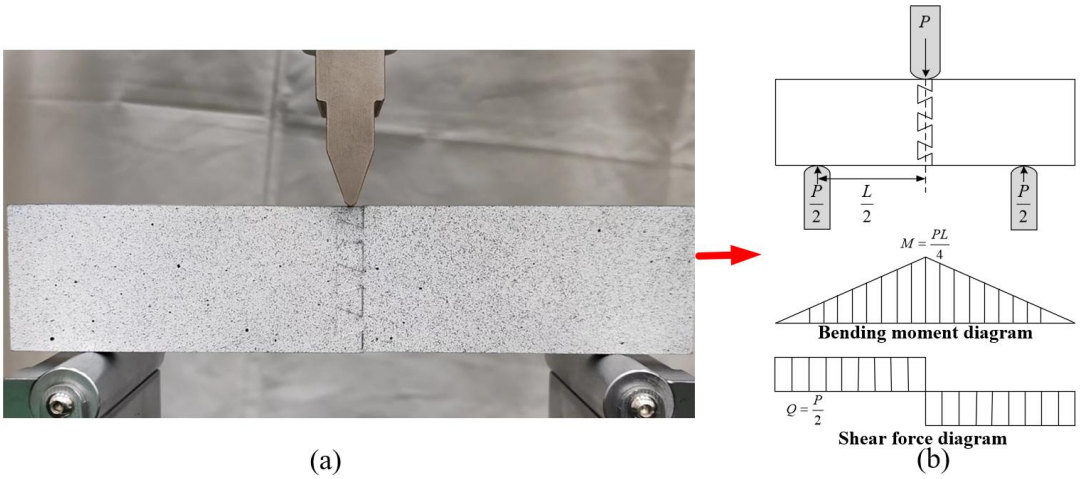

Figure 3 Test setup (a) three-point bending test diagram (b) bending moment diagram and shear diagram

3 Analysis of Test Results

3.1 Analysis of Four-Point Bending Results

Fig. 4(a) shows the load-displacement curve of specimen #C1 under four-point bending. When the load reaches the peak point A, according to Fig. 4(b), it can be seen that the common tenon far away from the indenter end will have debonding damage, and the local bulge near the indenter end will appear. As the head drops, the load plummets to point B. Fig. 4(c) shows that in addition to the desticking damage and increased deformation of the tenon, the shoulder and the female tenon near the indenter end are extruded to cause desticking, resulting in delamination damage. At the same time, it can be determined that a relatively mild drop before the load reaches point B is caused by the extrusion between the shoulder of the tenon and the tenon, and the continuous decline of the indenter increases the extrusion pressure and intensifies the layered failure, resulting in the sudden drop of the load again. When the load reaches point C, the load rise stage appears in section BC. According to Fig. 4(d), the middle tenon of the common tenon is obviously unsticking. It can be seen that the carrying capacity of the tenon at the left and right ends of the common tenon decreases after layered failure, which makes the middle tenon act as the main bearing force and causes the load to rise briefly. As the load continues to decrease, it can be seen that the main failure forms of the CD segment are the dissticking of the tenon and tenon, and the layered failure caused by the extrusion of the female tenon and shoulder. When point D is reached, it can be seen from Fig. 4(e) that the tenon far from the indenter end is pulled out, and it is interesting that the load does not sudden drop. According to the final failure of the structure shown in Fig. 16(a), it can be seen that before pulling out the tenon far from the indenter end, serious stratified failure occurred, resulting in loss of original carrying capacity, so there was no significant impact on load reduction. When the load reaches point E, it can be seen from Fig. 4(f) that the tenon in the middle of the tenon has been pulled out, and there are cracks in the tenon near the end of the indenter. First, it can be determined that the middle tenon acts as the main bearing force after the tenon is pulled out away from the indenter end. Secondly, according to the final failure situation of the structure, the load decreases sharply due to the continuous expansion of cracks causing the fracture of the tenon.

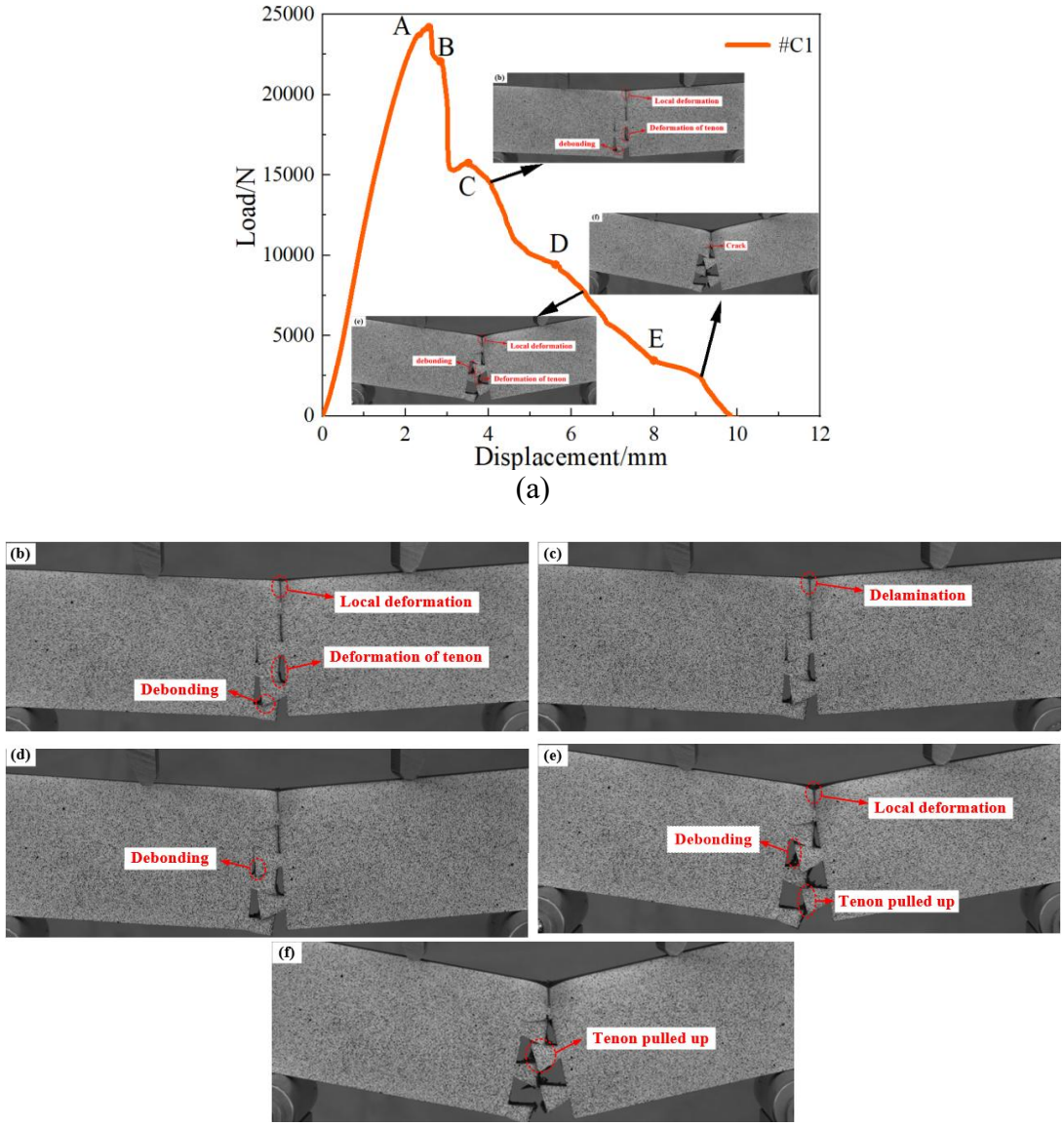

Figure 4 Four-point bending test of specimen #C1 (a) Load displacement curve (b) Structural damage at point A (c) Structural damage at point B (d) Structural damage at point C (e) Structural damage at point D (f) Structural damage at point E

Fig. 5(a) shows the load-displacement curve of specimen #C2. When the peak point A is reached, the main failure form is the unsticking of the male tenon and the middle tenon away from the indenter end. Then the load dropped dramatically. According to Fig. 5(b), it can be seen that debonding failure is still the main reason for the decrease of structural carrying capacity. When the load drops to point C, it can be seen from Fig. 5(c) that the tenon away from the indenter is pulled out. The situation of specimen #C2 is similar to that of specimen #C1, and no sudden drop of load occurs when the tenon is pulled out. The principle is the same as above, so I will not repeat it. However, it can be determined that the main failure mode of the BC section is the interlayer disbonding away from the end of the tenon and the middle of the tenon. The final load drops sharply at point D. According to Fig. 5(d), the tenon near the end of the indenter has a significant fiber fracture. Combined with Fig. 5(a), the fracture of the tenon is the main cause of the sudden drop in load.

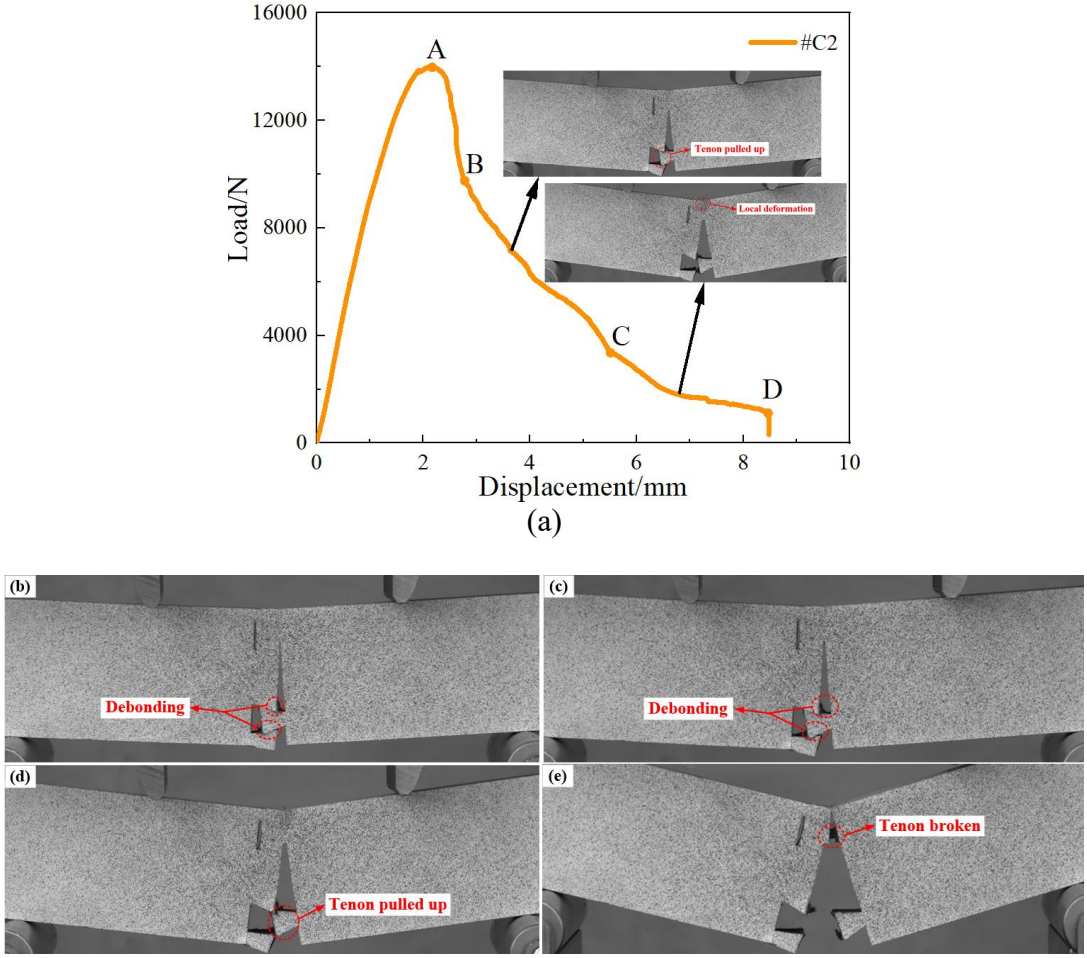

Figure 5 Four-point bending test of specimen #C2 (a) Load displacement curve (b) Structural damage at point A (c) Structural damage at point B (d) Structural damage at point C (e) Structural damage at point D

Fig. 6(a) shows the load-displacement curve of specimen #C3. When the load reaches the peak point A, the main failure form is still the unsticking of the tenon. As the indenter drops, the desticking phenomenon intensifies and the load decreases. According to Fig. 6(b), it can be seen that the shoulder and the female tenon are squeezed due to the pulling out of the tenon. Therefore, in the final failure situation, the tenon of specimen #C3 not only showed obvious layered failure, but also showed slight layered damage to the shoulder and tenon near the indenter end.

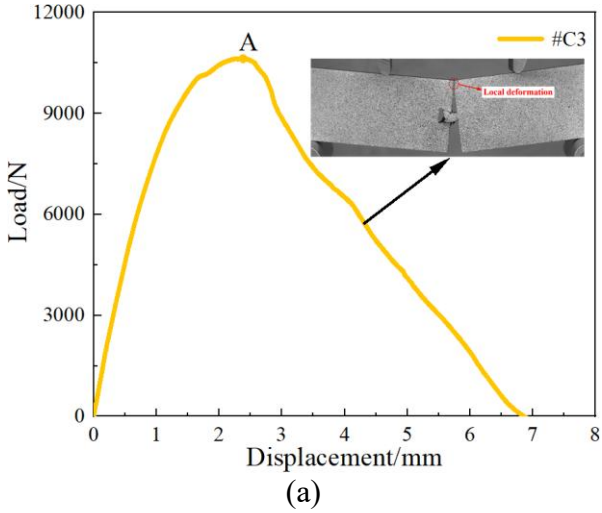

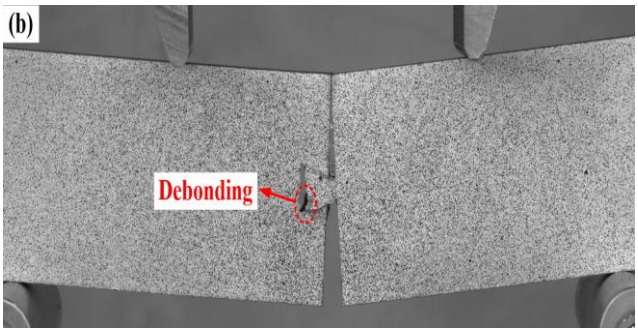

Figure 6 Four-point bending test for specimen #C3 (a) load-displacement curve (b) Structural damage at point A

Fig. 7-9 shows the DIC strain test results under four-point bending. It can be found that debonding is the main failure mode under the action of four-point bending. Therefore, the DIC analysis results of the three specimens at the moment when the debonding damage occurred were taken. At this time, the female mortise and tenon shoulder near the indenter end of the three specimens have a large compressive strain in the x direction. Therefore, this is the most vulnerable area for unbonding damage except for the tenon away from the indenter end, and all three specimens are compressive strains in the x direction away from the indenter end tenon. On the other hand, the y direction shows tensile strain. According to the strain-resolved cloud image in the xy direction, the resultant strain is the tensile strain. Therefore, the tensile deformation of the tenon under the action of four-point bending is the cause of the desticking damage in this part.

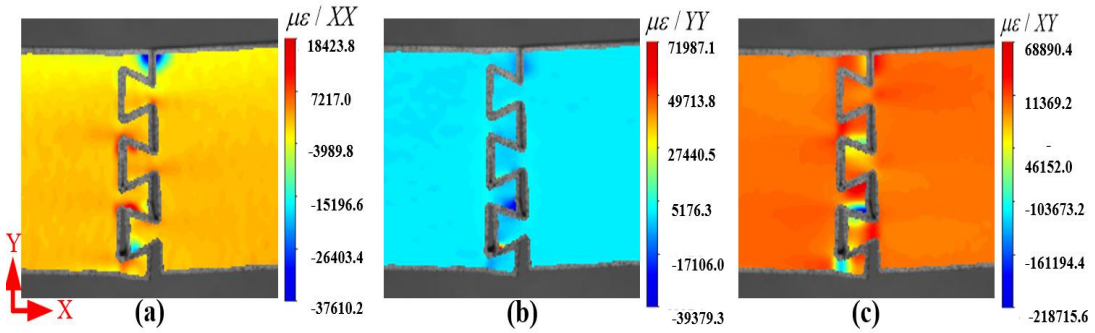

Figure 7 Analysis of DIC test results of four-point bending test of specimen #C1 (a) strain distribution cloud map in x direction (b) strain distribution cloud map in y direction (c) strain distribution cloud map in xy direction

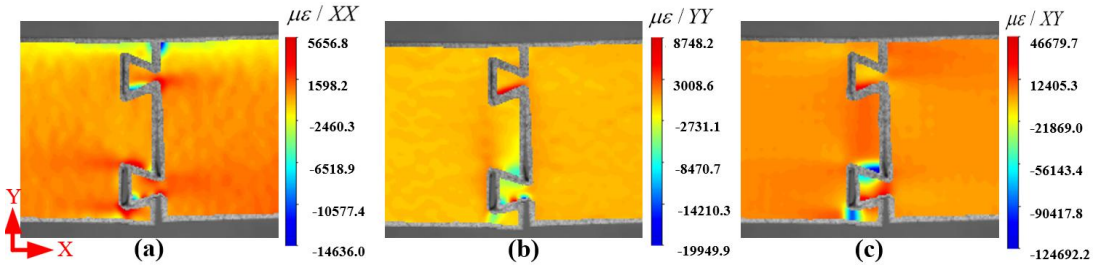

Figure 8 DIC test result analysis of specimen #C2 in four-point bending test (a) strain distribution cloud map in x direction (b) strain distribution cloud map in y direction (c) strain distribution cloud map in xy direction

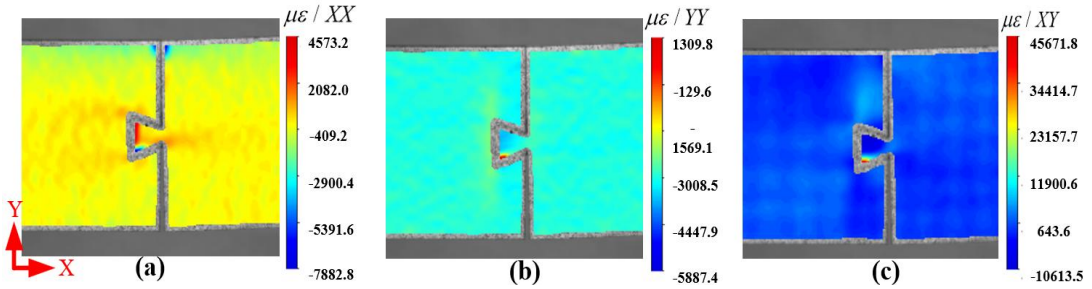

Figure 9 Analysis of DIC test results of four-point bending test of specimen #C3 (a) strain distribution cloud map in x direction (b) strain distribution cloud map in y direction (c) strain distribution cloud map in xy direction

3.2 Analysis of Three Point Bending Results

Fig. 10(a) shows the load-displacement curve of specimen #C1 under three-point bending. When the load reaches the peak point A, according to Fig. 10(b), the mortise and tenon away from the indenter end and the mortise at the pressure end are obviously detached. Therefore, the load drop is caused by the disadhesion damage. As the load descends to point B, a slight rise occurs. Observation of Fig. 10(c) shows that at this time, in addition to the aggravation of the debonding damage, the compression end of the tenon has a local bulge. It can be inferred that the pressure end of the mortise and tenon shoulder compression to some extent to alleviate the load drop, resulting in a temporary load rise. When the indenter continues to drop and the load reaches point C, observe Fig. 10(d). At this moment, the female tenon of the compression end appears layered damage and the male tenon cracks. It can be seen that the dominant failure mode of the CD segment is the lamination damage of the mortise on the pressure end due to serious debonding, while the stationary segment is caused by crack propagation. And then the load goes down to point D. As can be seen from Fig. 10(e), at this time, the tenon away from the indenter end is pulled out, resulting in a slight load drop. Meanwhile, according to Fig. 10(f), the dominant failure mode of section CD is crack propagation at the neck of the tenon. When the final load reaches point E, it plummets. According to Fig. 10(e), it is mainly caused by the fracture of the tenon in the middle of the tenon and the tenon near the indenter, and the dominant failure mode of the DE section is the crack propagation of the neck of the tenon in the middle of the tenon.

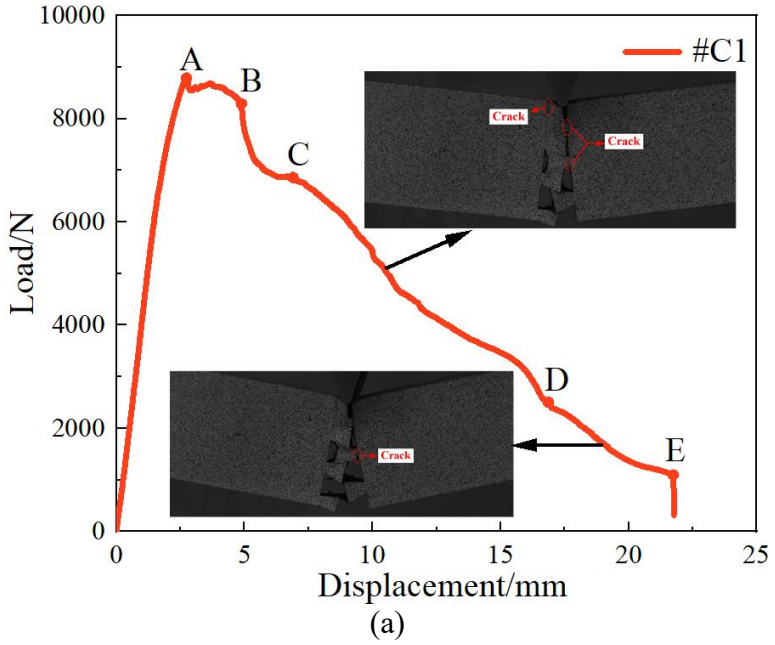

(a)

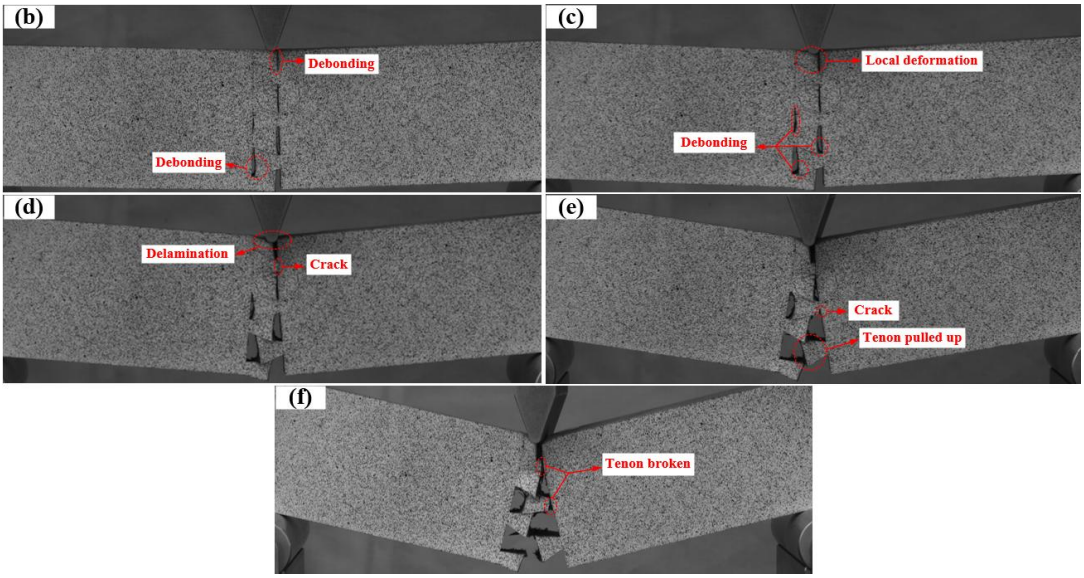

Figure 10 Three-point bending test of specimen #C1 (a) Load displacement curve (b) Structural damage at point A (c) Structural damage at point B (d) Structural damage at point C (e) Structural damage at point D (f) Structural damage at point E

Fig. 11(a) shows the load-displacement curve of specimen #C2. According to Fig. 11(b), when the load reaches the peak, the mortise near the indenter end and away from the indenter end have obvious dissticking phenomenon. When the load reaches point B, it can be seen from Fig. 11(c) that the mortise far away from the indenter end has obvious delamination due to debonding. Therefore, it can be concluded that the cause of load drop is still debonding. After passing point B, the load drop slows down. When point C is reached, it is found in Fig. 11(d) that the mortise and tenon shoulder near the indenter end are squeezed, resulting in local protruding. The indenter continues to drop and the load reaches point D. By observing Fig. 11(e), it is found that the tenon far from the indenter end is pulled out at this time, and the situation is similar to that of specimen #C1 without sudden load drop. Combined with Fig. 11(a), it can be seen that the dominant failure mode of section CD is the stratified failure near the mortise and tenon shoulder of the indenter end and the disbonding of the mortise and tenon away from the indenter end.

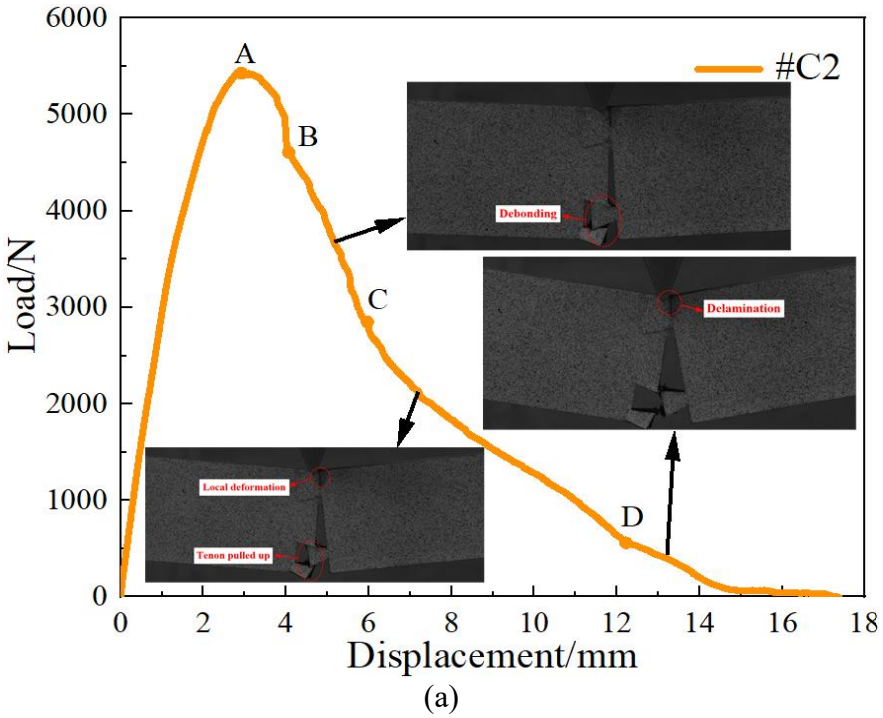

(a)

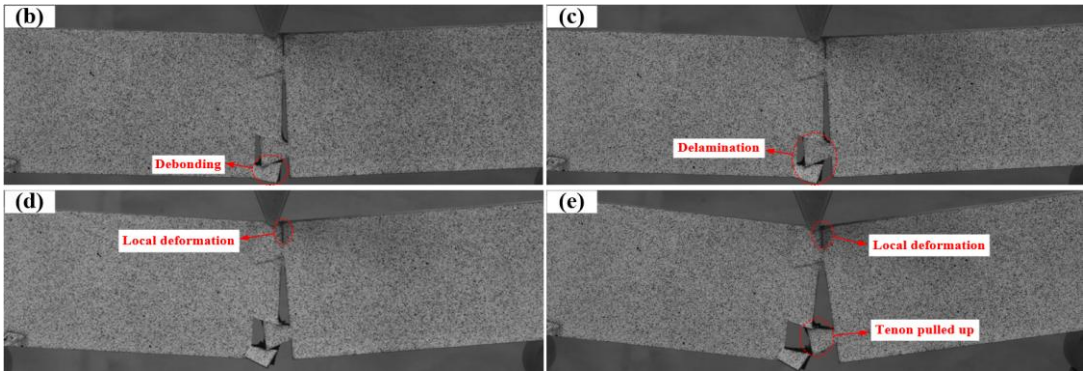

Figure 11 Three-point bending test of specimen #C2 (a) Load displacement curve (b) Structural damage at point A (c) Structural damage at point B (d) Structural damage at point C (e) Structural damage at point D

Fig. 12(a) shows the load-displacement curve of specimen #C3. When the load reaches the peak point A, the mortise and tenon have the phenomenon of unsticking. As the indenter descends, the mortise and tenon shoulder near the indenter end compresses. At point B, the tenon basically loses its carrying capacity. Next near the end of the indenter, the mortise and tenon shoulder squeeze each other to act as the main bearing force. Finally, according to the final failure mode of three-point bending in Fig. 16(b), the tenon fracture and serious layered failure occurred in specimen #C1. However, specimens #C2 and #C3 mainly failed in stratification and did not fully exert the load-bearing performance of the tenon. Therefore, the design of multi-tenon can give full play to the mechanical properties of dovetail tenon.

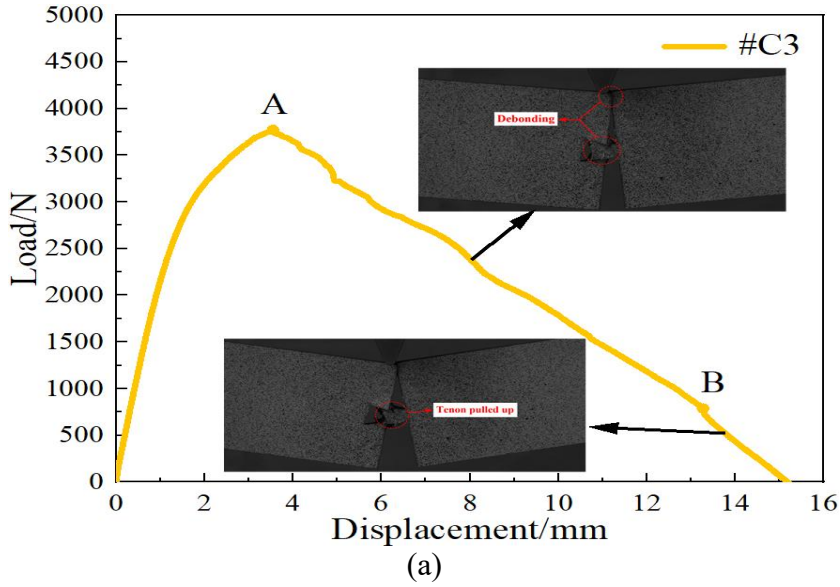

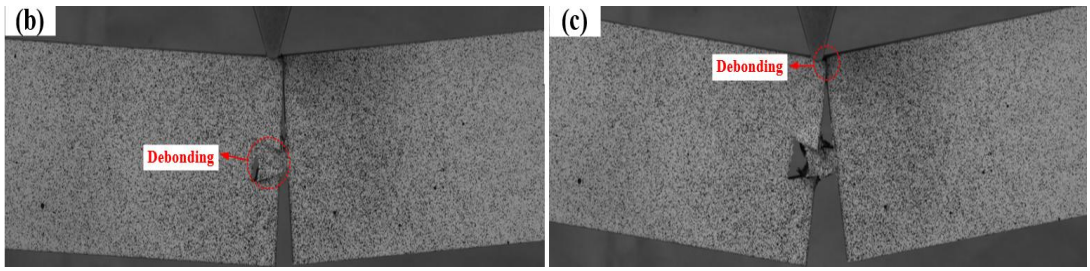

Figure 12 Three-point bending test of specimen #C3 (a) Load displacement curve (b) Structural damage at point A position (c) Structural damage at point B position

Fig. 13-15 shows the DIC strain test results under four-point bending. In the same way, DIC strain nephogram at the moment when the structure has just appeared disadhesion damage is taken for

analysis. Under the action of three-point bending, obvious compressive strain also appeared in the three specimens near the end of the indenter. It was also caused by the pressing of the mortise and tenon shoulder. Different from the pure bending action, the tenon far away from the indenter shows tensile strain in the x direction, compressive strain in the y direction, and tensile strain in the combined strain. Therefore, no matter it is four-point bending or three-point bending, the desticking damage is caused by the tensile deformation of the tenon.

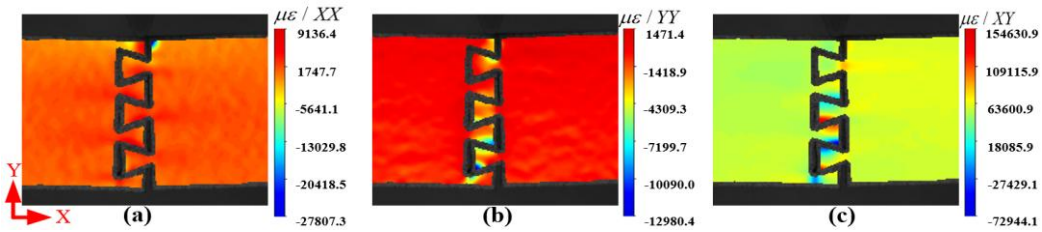

Figure 13 Analysis of DIC test results of three-point bending test of specimen #C1 (a) strain distribution cloud map in x direction (b) strain distribution cloud map in y direction (c) strain distribution cloud map in xy direction

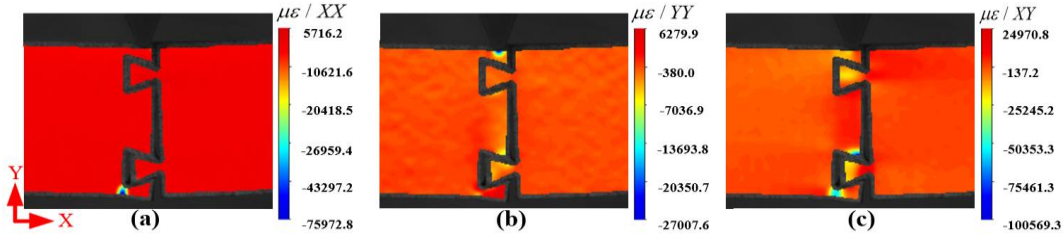

Figure 14 DIC test results of three-point bending test of specimen #C2 were analyzed for (a) strain distribution cloud map in x direction (b) strain distribution cloud map in y direction (c) strain distribution cloud map in xy direction

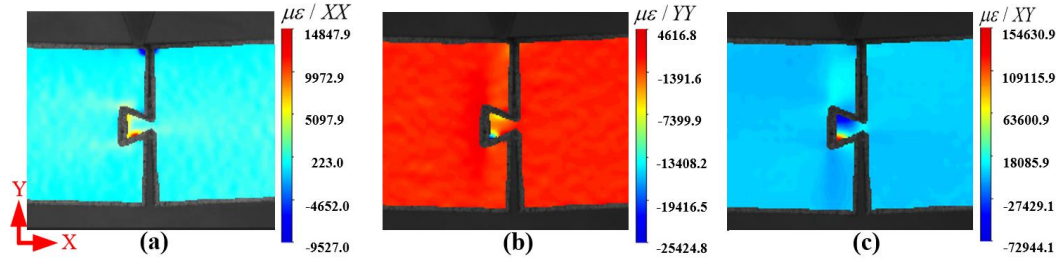

Figure 15 DIC test results analysis of specimen #C3's three-point bending test (a) strain distribution cloud map in the x direction (b) strain distribution cloud map in the y direction (c) strain distribution cloud map in the xy direction

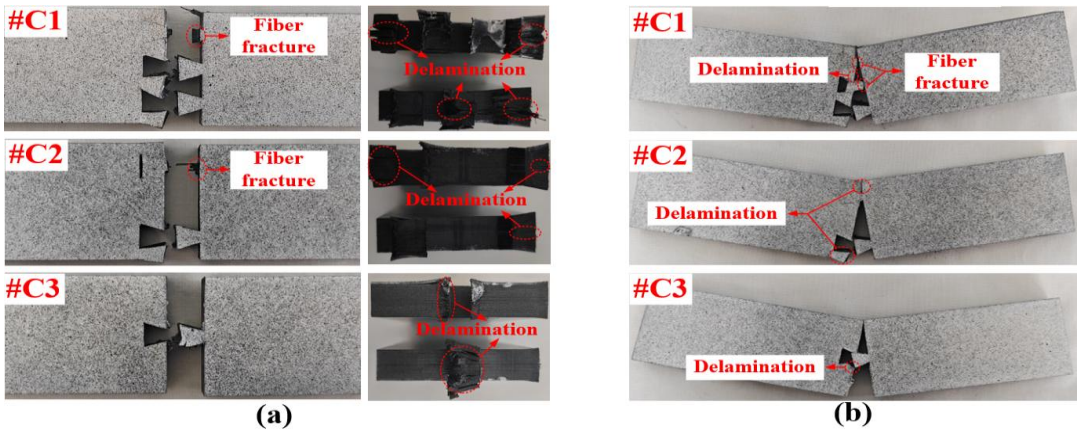

Figure 16 Final failure result (a) four-point bending test (b) three-point bending test

4 Simulation Analysis of Bending of CFRP Multi-Dovetail Joint

4.1 Damage Initiation and Damage Criterion

In order to determine the damage initial of various damage modes between layers of composite materials and evaluate the effective stress state during loading, stress risk coefficient was used to characterize the damage initial of various modes:

$$f\left(F_I, r_I\right) = F_I - r_I = 0; I = \{\text{ft,fc,m}\} \tag{5}$$

In the formula: F_I is the loading function of different failure modes; r_I is the damage threshold, and the initial value is 0. When $r_I = 1$, the material damage is defined; When $r_I > 1$, the damage development of the material is defined. Using LaRC05 criterion as the damage failure criterion of carbon fiber composites, it is mainly divided into fiber tensile failure, fiber compression failure (fiber kinking, fiber splitting) and matrix cracking. So ft,fc,m stands for fiber tensile failure, fiber compression failure (fiber kinking, fiber splitting), and matrix cracking respectively.

Fiber tensile failure:

$$F_{\text{ft}} = \frac{\overline{\sigma}_{11}}{X_{\text{T}}}, (\overline{\sigma}_{11} \geq 0) \tag{6}$$

Fiber compression failure (fiber kink) :

$$F_{\text{KINK}} = \left(\frac{\overline{\tau}_{23}^{\varphi}}{S_{\text{T}} - \eta_{\text{T}}\overline{\sigma}_2^{\varphi}}\right)^2 + \left(\frac{\overline{\tau}_{12}^{\varphi}}{S_{\text{L}} - \eta_{\text{L}}\overline{\sigma}_2^{\varphi}}\right)^2 + \left(\frac{\left\langle \overline{\sigma}_{22}^{\varphi} \right\rangle}{Y_{\text{T}}}\right)^2, \left(\left|\overline{\sigma}_{11}\right| \geq \frac{X_C}{2}\right) \tag{7}$$

Fiber compression failure (fiber splitting) :

$$F_{\text{SPLIT}} = \left(\frac{\overline{\tau}_{23}^{\varphi}}{S_{\text{T}} - \eta_{\text{T}}\overline{\sigma}_2^{\varphi}}\right)^2 + \left(\frac{\overline{\tau}_{12}^{\varphi}}{S_{\text{L}} - \eta_{\text{L}}\overline{\sigma}_2^{\varphi}}\right)^2 + \left(\frac{\left\langle \overline{\sigma}_{22}^{\varphi} \right\rangle}{Y_{\text{T}}}\right)^2, \left(\left|\overline{\sigma}_{11}\right| < \frac{X_C}{2}\right) \tag{8}$$

Matrix cracking

$$F_{\text{m}} = \left(\frac{\overline{\tau}_L}{S_{\text{L}} - \eta_{\text{L}}\overline{\sigma}_N}\right)^2 + \left(\frac{\overline{\tau}_T}{S_{\text{T}} - \eta_{\text{T}}\overline{\sigma}_N}\right)^2 + \left(\frac{\left\langle \sigma_N \right\rangle_+}{Y_{\text{T}}}\right)^2 \tag{9}$$

In the formula, S_{L} and S_{T} are the fiber direction and transverse shear strength along the fracture plane of the matrix respectively. Y_{T} is the transverse tensile strength; η_{L} and η_{T} are the longitudinal and transverse shear friction coefficients, respectively. X_C is the longitudinal compressive strength; $\overline{\tau}_{12}^{\varphi}, \overline{\tau}_{23}^{\varphi}$, and $\overline{\sigma}_{22}^{\varphi}$ are the stresses in the direction of fiber kinking when fiber kinking/splitting occurs, respectively.

4.2 Damage Evolution

When the damage threshold $r_I > 1$, the material damage begins to expand. Due to the gradual increase of effective stress, material damage will

be further aggravated. The mechanical properties of the material are degraded and the bearing capacity is decreased. A linear progressive reduction scheme is used to describe the damage evolution of the material：

$$d_I = \max\left\{0, \min\left\{d^*, \frac{\varepsilon_{\mathrm{eq,f}}^I\left(\varepsilon_{\mathrm{eq}}^I - \varepsilon_{\mathrm{eq,0}}^I\right)}{\varepsilon_{\mathrm{eq}}^I\left(\varepsilon_{\mathrm{eq,f}}^I - \varepsilon_{\mathrm{eq,0}}^I\right)}\right\}\right\}; I = \{\mathrm{ft,fc,m}\} \quad (10)$$

In the formula, d_I is the damage state variable; d_{ft},d_{fc}, and d_m were the damage variables of fiber stretching, fiber compression and matrix cracking, respectively. When the material is not damaged, d_I =0; When the material completely fails, d_I =1, in order to prevent the stiffness from being reduced to 0 in the finite element calculation process, resulting in the singularity of the material stiffness matrix. Set $d^* = 0.99$; $\varepsilon_{\mathrm{eq}}^I$ is the equivalent strain; $\varepsilon_{\mathrm{eq,0}}^I$ is the equivalent strain when the initial damage occurs. $\varepsilon_{\mathrm{eq,f}}^I$ is the equivalent strain at complete failure.

4.3 Interlayer Damage Model

According to the final failure results of the four-point bending and three-point bending tests in Fig. 16, it can be seen that the desticking and delamination caused by larger external forces are still the main damage types. The damage model of the rubber layer between carbon fiber layers is briefly introduced below [32, 33]. The bilinear constitutive model of the Cohesive force element is generally adopted when the stress is proportional to the strain. The Cohesive thickness between carbon fiber layers can be defined as 0.1mm. Based on B-K fracture and force-separation displacement criteria, a continuous damage mechanism was established in the unit between the carbon fiber and the adhesive layer. The debonding failure is simulated by Cohesive cohesive interface unit simulation. The constitutive relation is as follows:

$$t = \begin{Bmatrix} t_n \\ t_s \\ t_t \end{Bmatrix} = \begin{bmatrix} K_{nn} & 0 & 0 \\ 0 & K_{ss} & 0 \\ 0 & 0 & K_{tt} \end{bmatrix} \begin{Bmatrix} \varepsilon_n \\ \varepsilon_s \\ \varepsilon_t \end{Bmatrix} = K\varepsilon \quad (1)$$

In formula (1), the normal stress of the viscous interface element and the internal shear stress on two different surfaces are represented, respectively. $\varepsilon_i = \delta_i / T_0 (\mathrm{i = n,s,t})$, T_0 is the thickness of the Cohesive unit actually modeled. δ_i is the relative displacement of Cohesive on the corresponding direction of the top and bottom surface of the unit; K_{ii} is the stiffness coefficient. The secondary stress criterion is used as the damage initiation criterion:

$$\left(\frac{t_n}{t_n^0}\right)^2 + \left(\frac{t_s}{t_s^0}\right)^2 + \left(\frac{t_t}{t_t^0}\right)^2 = 1 \quad (2)$$

In formula (2), t_n^0、t_s^0、t_t^0 are the normal stress and two in-plane shear stresses of the interlayer and rubber layer elements. When the above formula is true, the Cohesive unit fails. When the Cohesive element is damaged, its constitutive relation is as follows:

$$t = (1 - D)\mathrm{diag}(K_{\mathrm{nn}}, K_{ss}, K_{\mathrm{tt}})\delta_i \quad (3)$$

In formula (3), the damage coefficient of the cohesive layer, with a range of [0,1]; when $D = 0$, there is no failure of the cohesive layer; When $D = 1$, the viscous layer completely fails. The process of stiffness degradation and final failure displacement of the material is mastered by the element critical strain energy release rate G_{C}. The failure process of the Cohesive element is

calculated by the B-K fracture criterion.

$$G^{C} = G_{n}^{C} + (G_{s}^{C} - G_{n}^{C})(\frac{G_{S}}{G_{T}})^{\eta} \quad (4)$$

In formula (4), $G_{S} = G_{s} + G_{t}; G_{T} = G_{n} + G_{s}; G_{n}^{C}, G_{s}^{C}, G_{t}^{C}$ are the critical fracture energies in the normal direction and two shear directions, respectively. η is related to material parameters. When the material is carbon fiber reinforced epoxy resin composite material, $\eta = 1 \sim 2$, $\eta = 1.8$ is adopted in this paper.

4.4 CFRP Multi-Dovetail Joint Bending Simulation Model

Fig. 17 is a simulation model of three-point bending (3PB) and four-point bending (4PB) tests established by ABAQUS. The modeling details in Fig. 17(a) are as follows. Set the indenter and support as rigid bodies respectively, fix the support, and remove the constraint on the y axis direction of the indenter. The displacement distance of the model indenter is determined according to the actual displacement of the test. Set the universal contact, use "penalty" contact for tangential and set the coefficient of friction to 0.3, and use "hard" contact for normal. Due to the obvious dissticking phenomenon in the test, in order to better simulation analysis, the joint is taken as an example in Fig. 17(b). With the same mortise, ten layers of carbon fiber (thickness of 1mm) are established. Giving material properties to T300/ epoxy composite prepreg. Insert an adhesive layer (thickness 0.1mm) between layers. Give LJM-170 material properties. SC8R unit and Cohesive unit are used respectively, and a total of 193,420 units are divided. Finally, the carbon fiber layer and the rubber layer are set as binding constraints.

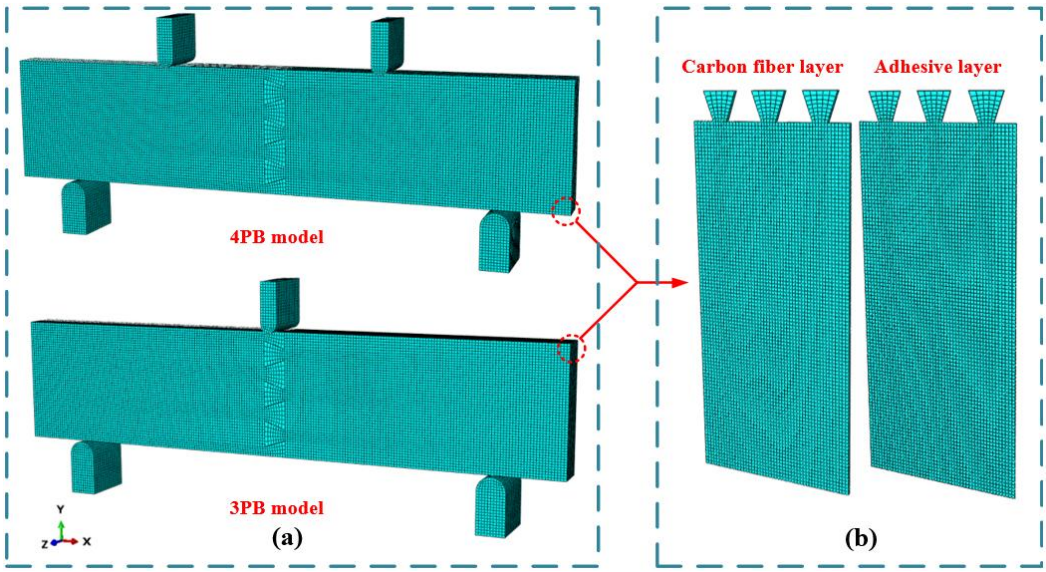

Figure 17 Simulation model (a) four - and three-point bending test (b) carbon fiber layer (dowel) and adhesive layer

4.5 Comparative Analysis of Bending Test and Simulation Results

Fig. 18 shows the comparison of the 4PB and 3PB test and simulation results. According to the comparison between the load displacement curve of the test and simulation in Fig. 19, the load is taken to rise linearly to the peak stage (this section is selected because after the load reaches the peak, the structure will significantly destick, which will affect the accuracy of strain cloud image in DIC test. Simulation results cannot be compared. First, the results of the 4PB test and simulation are selected for analysis. At point A, the structure has just become unglued, as shown in Fig. 18(a). According to (2), it can be seen that at this time, the common tenon far from the indenter end appears unstuck for the first time. By comparison

(4), it can be found that the cohesive force model of the simulation model is damaged at this position, which is also manifested as debonding. Meanwhile, the displacement cloud image (1) obtained by the DIC strain testing system is similar to the simulated displacement cloud image (3). When the load reaches the peak point B, it can be seen from Fig. 18(b) that the mortise joints near and far from the indenter end in test (2) are unglued. Compared with simulation (4), the cohesive force model near the indenter end has been deleted due to unit failure. The failure conditions of the test and simulation are well compared. The displacement cloud image (1) of the DIC strain testing system is not much different from the simulated displacement cloud image (3). Then the 3PB test and simulation results are analyzed. At point C, it can be seen from Fig. 18(c) that the mortise near the end of the indenter appears for the first time in test (2). In the simulation (4), cohesive force model damage also occurs at the same position. When the load reaches the peak point D, as shown in Fig. 18(d), the position of the debonding damage in test (3) is the same as that in the 4PB test at the peak point. Simulation (4) also corresponds well to experiment (3), and the DIC strain test displacement cloud image obtained at two points C and D is in good agreement with the simulation displacement cloud image. The peak error of the 3PB and 4PB tests and simulations is within ±8%, which verifies the validity of the simulation model.

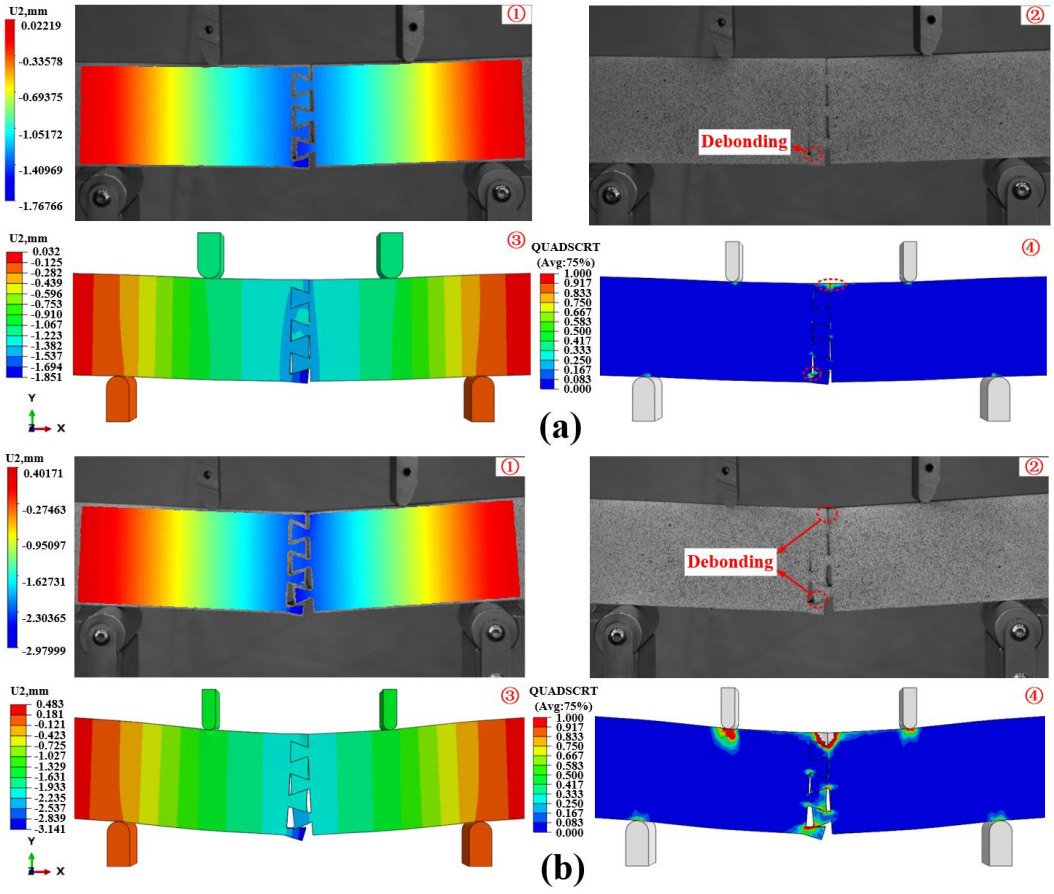

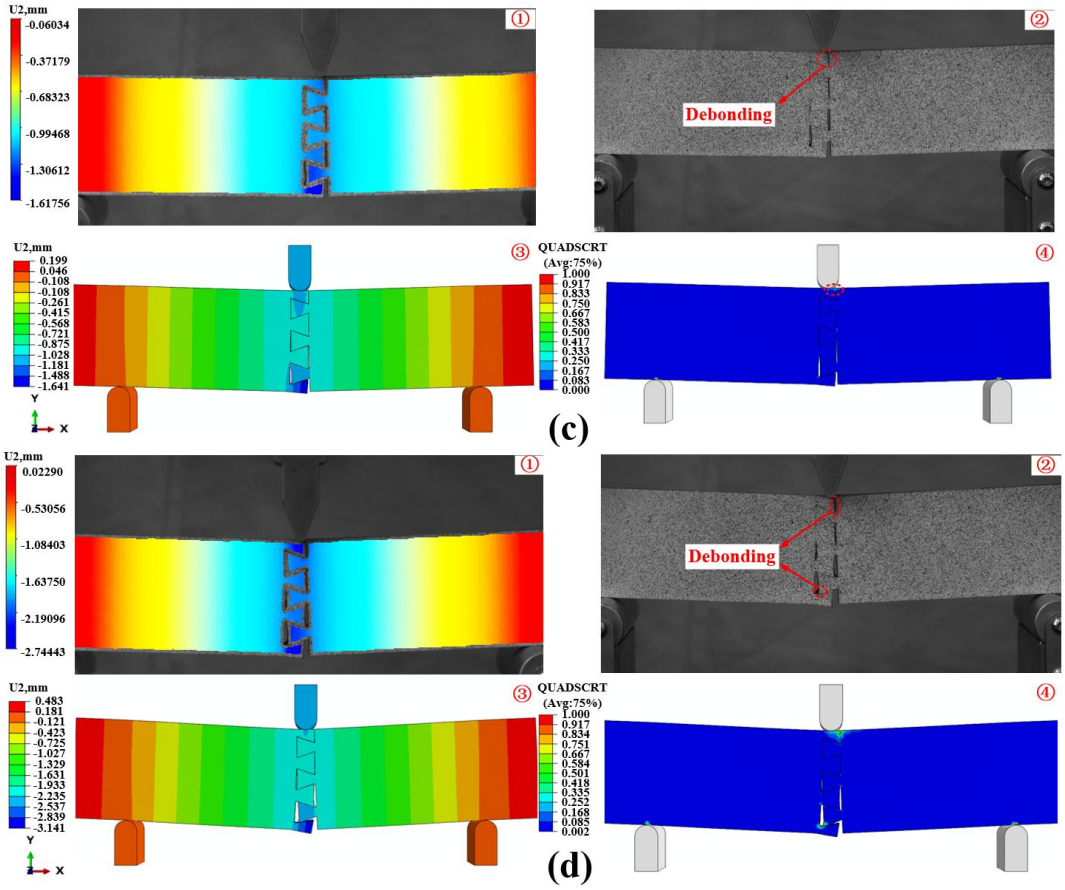

Figure 18 Comparison between simulation and experiment (a) Structural deformation at the position of point A (b) Structural deformation at the position of point B (c) Structural deformation at the position of point C (d) Structural deformation at the position of point D

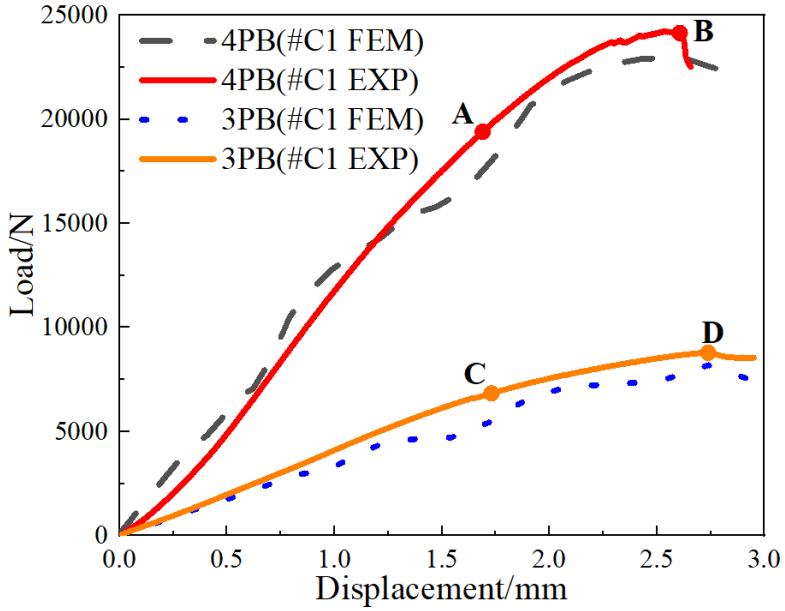

Figure 19 Comparison of load displacement curves of 4PB and 3PB test and simulation results

According to the final failure results of the structure in Fig. 16, it can be found that debonding is the most important failure mode, but the position where debonding first occurs cannot be determined during the bending test. After the verification, the cohesive layer of the model is extracted and analyzed, as shown in Fig. 20. It is easily found that during the bending test, both

four-point and three-point bending, the damage on the outside cohesive layer leads to unit deletion, while the damage on the inside cohesive layer does not lead to obvious unit deletion. Compared with three-point bending, four-point bending is more likely to cause debonding damage. Therefore, the bending resistance of the structure can be improved by increasing the bonding strength of the outer viscous layer.

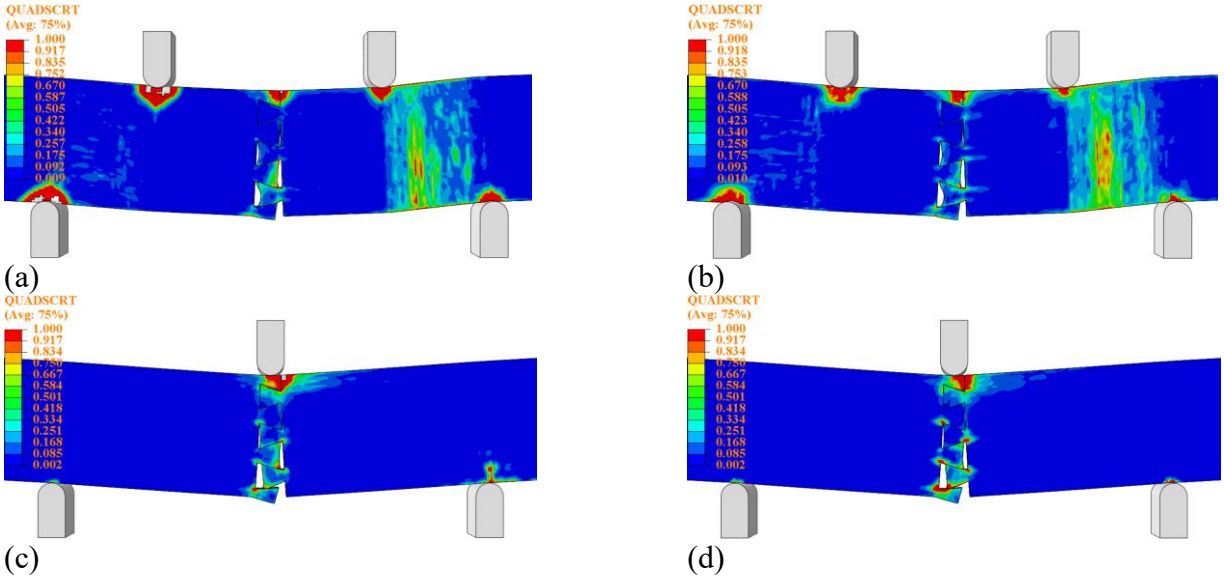

Figure 20 Four-point bending: (a) outer cohesive cell layer (b) inner cohesive cell layer; Three-point bending (c) outer cohesive element layer (d) inner cohesive element layer

4.6 The Effect of Paving on the Structure

Through the verified simulation model, since the debonding damage is more obvious in the four-point bending test, the damage type is easier to observe and select this model to analyze the influence of layering parameters on the dovetail structure of CFRP. Table 2 below shows the design of four common layering parameters.

Table 2 Simulation model of four different layering methods

model	Lay-up mode
C1’	$[0/90]_{25}$
C2’	$[\pm45]_{25}$
C3’	$[90]_{50}$
C4’	$[0]_{50}$

The stress distribution nephograms of the four models were analyzed when the desticking damage occurred. As shown in Fig. 21, it can be found that the stress distribution of the four models is related to the layup direction. And basically concentrated distribution away from the head end of the tenon near. Therefore, the three-dimensional strain cloud image at this position was extracted for analysis. As shown in Fig. 22(a), the strain is selected from the lower end of the tenon. It is found that the maximum strain of C1’, C3’and models all appear at the lower end of the tenon. This is also the main reason why this location is most prone to debonding damage. However, the position of the maximum strain of C2 ’ is shifted back. It seems that the lay-up mode can not only determine the direction of stress distribution but also change the location of maximum strain. Among the four models, the maximum strain of model C3 ’ is the smallest, followed by C1 and C2 ’ is the largest. According to their respective stress distribution cloud maps, C1 and C3’s strain is not large when the stress concentration is relatively serious, which indicates

that 90° paving can improve the strength of the structure to a certain extent.

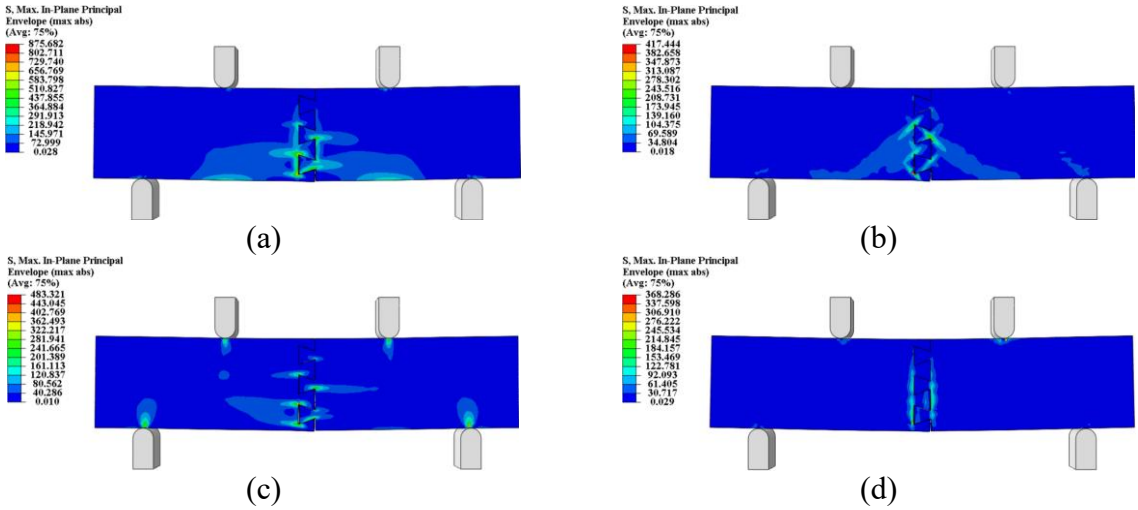

Figure 21 stress distribution program (a) $[0/90°]_{25}$ (b) $[\pm45°]_{25}$ (c) $[90°]_{50}$ (d) $[0°]_{50}$

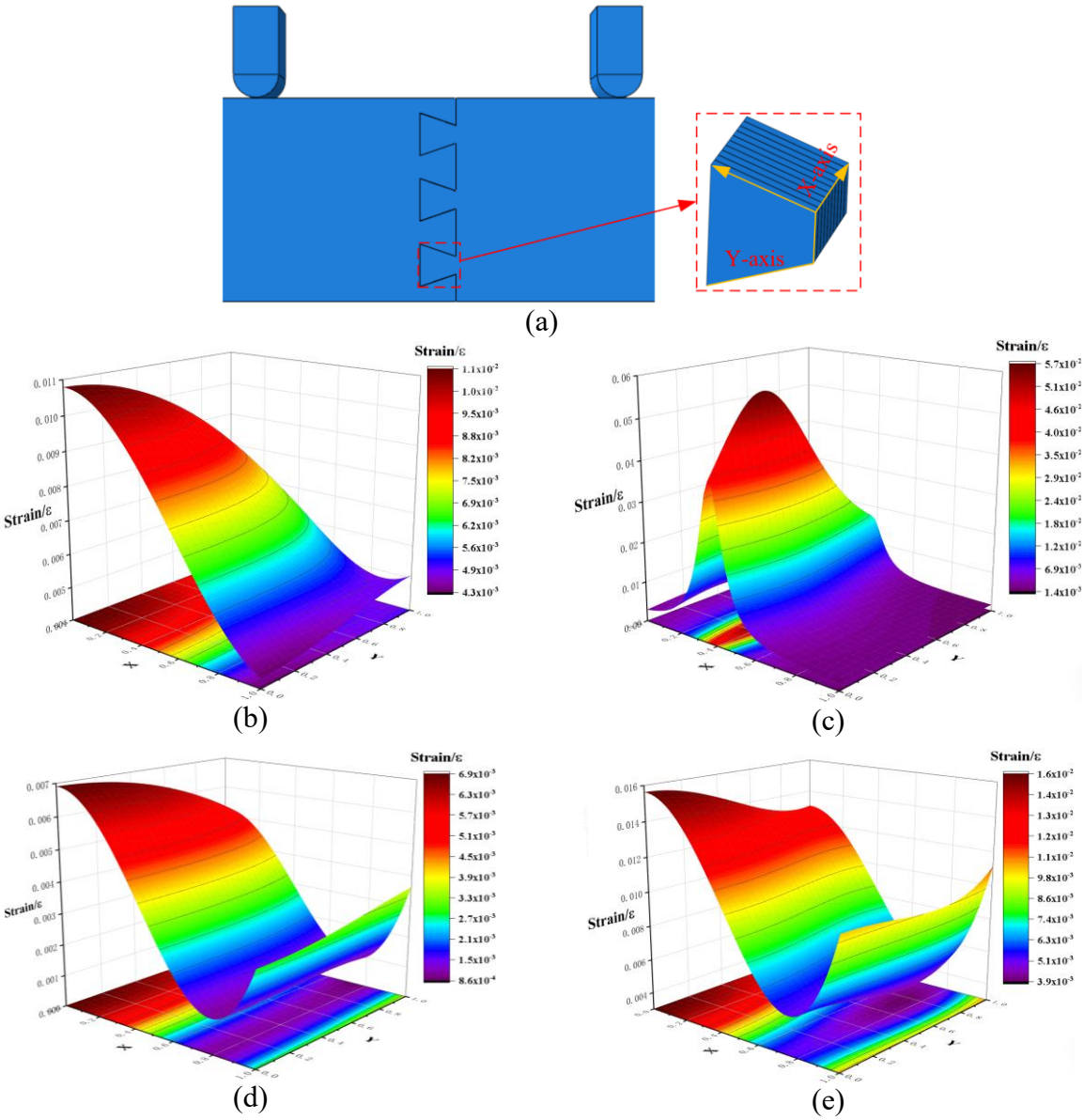

Figure 22 Three-dimensional strain diagram (a) Schematic diagram (b) $[0/90°]_{25}$ (c) $[\pm45°]_{25}$ (d) $[90°]_{50}$ (e) $[0°]_{50}$

5 Conclusion

In this paper, four-point and three-point bending tests of CFRP dovetail structures with different numbers of tenons are carried out. The damage mechanism of the structure under bending was analyzed according to DIC strain test results. Combined with the verified finite element simulation model, the influence of different layering on the bending properties of the structure is discussed. Specific conclusions are as follows:

(1) Under the action of bending, the outer surface of the structure will be the first to show adhesive damage. With the gradual increase of bending load, the degree of debonding increases, which leads to delamination damage. Eventually, the structure will show fiber fracture damage. The analysis shows that stratified failure is the key factor that causes the structural bending property to decline. Therefore, in order to improve the bending property of the structure, the interlayer bond strength of the carbon fiber can be emphasized. This method is expected to provide an effective way to enhance the performance of the structure under bending conditions.

(2) According to DIC strain test results, in bending action, the joint strain of the tenon far away from and close to the indenter end is tensile strain. This phenomenon shows that the tensile strain is the main deformation mode of the structure under bending conditions. Further analysis shows that the mechanism of the desticking damage is that the tenon is squeezed by the mortise during the drawing process, which leads to the tensile deformation and finally the appearance of the desticking damage. This conclusion is of great significance for further understanding of the mechanical behavior and damage mechanism of the structure in the bending state.

(3) By comparing and analyzing the displacement nephogram, load-displacement curve and maximum peak load obtained by experiment and simulation, the validity of the simulation model is effectively verified. Based on the in-depth analysis of the simulation model after verification, it can be seen that the damage to the external cohesive layer is often the first to occur during the bending action. Therefore, the overall performance of the structure can be improved by enhancing the strength of the external viscous layer. Further to [0/90 °] $_{2\ 5}$, [plus or minus 45 °] $_{2\ 5}$, [90 °] $_{5}$ zero, [0 °] $_{5}$ zero this four different layer Angle analysis, the results show that the stress distribution is closely related to the direction of each layer. In particular, the addition of 90° paving significantly improves the bending properties of the structure. This research conclusion provides an important theoretical basis and practical guidance for the optimization design of relevant structures, which is helpful to choose the layup Angle more reasonably in practical engineering applications, and then improve the performance of structures under bending conditions.

Based on the mechanical behavior of CFRP dovetail structure under the bending action of air-dropped equipment, this paper further strengthens the comprehensive effectiveness of equipment support, extends the connotation of air-dropped equipment support, and gives full play to the role of equipment support as a multiplier of combat effectiveness and efficiency of rescue teams. In the process of researching the equipment support material and structure of the airdrop equipment, the design concepts of carbon fiber composite material and mortise and tenon structure are innovatively applied by drawing on the traditional wisdom. It can improve the efficiency and flexibility of equipment support. Combined with the research data, it can provide empirical support for the construction of equipment support model, the peacetime and war transformation of equipment support system, and the command and decision of equipment support. The wide application of stable and reliable mortise and tenon structure can promote the implementation of autonomous airdrop equipment support. Ensuring the continuous and stable output of the team during the execution of tasks can win more initiative for the emergency team in the future rescue and expand greater space for innovation.

6 Declaration of Interest Statement

The authors declare that they have no known competing financial interests or personal relationships that could have appeared to influence the work reported in this paper.

References

1. Moehrle M G, Frischkorn J. Bridge strongly o r focus – An analysis of bridging patents in fo ur application fields of carbon fiber reinforce

ments [J]. Journal of Informetrics, 2021,15 (2) .
2. Xia Y, Mu T, Liu Y, et al. Harnessing the powe r of carbon fiber reinforced liquid crystal elast omer composites for high-performance aerosp ace materials: A comprehensive investigation on reversible transformation and shape memor y deformation [J]. Composites Part A: Applied Science and Manufacturing, 2024, 177.
3. Papavassiliou A, Pavlovic A, Minak G. Crash worthiness investigation on a Carbon Fiber Re inforced Plastic solar vehicle [J]. Composite S tructures, 2024, 340.
4. Kim J, Yun H, Won S, et al. Comparative degr adation behavior of polybutylene succinate (P BS), used PBS, and PBS/Polyhydroxyalkanoat es (PHA) blend fibers in compost and marine–sediment interfaces [J]. Sustainable Materials and Technologies, 2024, 41.
5. Xu W, Wang D. Fatigue/impact analysis and st ructure–connection–performance integration multi-objective optimization of a bolted carbo n fiber reinforced polymer/aluminum assembl ed wheel [J]. Composites Part B: Engineering, 2022, 243.
6. Zhong S, Li H, Yang L, et al. Fatigue failure b ehaviour of bolted joining of carbon fibre reinf orced polymers to titanium alloy [J]. Engineeri ng Failure Analysis, 2024, 163.
7. Girão Coelho A M, Mottram J T. A review of t he behaviour and analysis of bolted connectio ns and joints in pultruded fibre reinforced poly mers [J]. Materials & Design, 2015,74:86-107.
8. Scattina A, Roncato D, Belingardi G, et al. Inv estigation of creep phenomenon on composite material for bolt connections [J]. Composite St ructures, 2015, 134: 378-383.
9. Liu K, Liu Y, Sabbrojjaman M, et al. Effect of bolt size on the bearing strength of bolt-conne cted orthotropic CFRP laminate [J]. Polymer T esting, 2023, 118: 107894-107905.
10. Liu Y, Wu Q, Wang P, et al. Forming process p rediction of a self-piercing riveted joint in carb on fibre reinforced composites and aluminium alloy based on deep learning [J]. Journal of M anufacturing Processes, 2023, 106: 453-464.
11. Huang Z-C, Li H-Z, Jiang Y-Q. Low-velocity impact response of self-piercing riveted carbo n fiber reinforced polymer-AA6061T651 hybr id joints [J]. Composite Structures, 2023, 315.
12. Zhuang W, Chen S, Liu Y. Influence of joining temperature on damage of warm self-piercing riveted joints in carbon fiber reinforced polym er and aluminum alloy sheets [J]. Journal of M anufacturing Processes, 2023, 89: 77-91.
13. Atta A M, Behiry R N, Haraz M I. Upgrading t he hanger resistance of RC inverted T-girders using externally bonded carbon fiber reinforce d polymers (EB-CFRP) [J]. Structures, 2023, 53:1557-1581.
14. Li Z, Qian Y, Li T, et al. The mechanical respo nses of SiC-coated carbon-bonded carbon fibe r composites under quasi-static cyclic compres sive loading [J]. Composites Part B: Engineeri ng, 2024, 283.
15. Najafgholipour M A, Saeid Kalantari Kouhban ani S, Peykari K. Experimental study on debo nding and buckling of externally bonded carbo n fiber reinforced polymer sheets in compressi on [J]. Engineering Failure Analysis, 2024,16 3.
16. Wang X, Jia X, Shi B, et al. Lightweight and t hermally insulating carbon-bonded carbon fibe r/graphite composite with enhanced in-plane h eat-leading functionality for efficient thermal protection materials [J]. Composites Communi cations, 2024, 51.
17. Çalık A, Akpinar S. The effect of fiber length and structure on joint strength in bonded joints with fiber-reinforced composite adhesive [J]. I nternational Journal of Adhesion and Adhesive s, 2023, 124: 103365-103373.
18. Ashong A N, Lee Y S, Park K S, et al. Effect o f HF treatment on the bonding strength of lase r-bonded Mg alloy/carbon fiber-reinforced pla stic joint: XPS and NEXAFS study [J]. Applie d Surface Science, 2021, 556: 149782-149786.
19. Sun C, Jia P, Chen C, et al. The effect of carbo n fibre stitching on the tensile behaviour of sec ondary bonded single- and double-lap compos ite joints [J]. Composite Structures, 2021, 265: 113774-113786.
20. Whitehouse A D, Médeau V, Mencattelli L, et al. A novel profiling concept leading to a signi ficant increase in the mechanical performance of metal to composite adhesive joints [J]. Com posites Part B: Engineering, 2023, 261: 11079 1-110805.
21. He J, Liu K, Xie L, et al. Experimental and nu merical studies on influences of wedge reinfor cement on seismic performance of loose penet rated mortise-tenon joints [J]. Journal of Build ing Engineering, 2024, 91: 109610-109631.
22. Wu H, Lu Z. Study on double dovetail tenon a

nd mortise combination of corn stalk biomass bricks [J]. Construction and Building Materials, 2023, 370: 130651-130659.
23. Wu Y-J, Wang L, Lin H-S, et al. Effect of shear force on the rotational performance of straight mortise-tenon joints [J]. Structures, 2022, 41: 501-510.
24. Yang Q, Yu P, Law S-S. Load resisting mechanism of the mortise-tenon connection with gaps under in-plane forces and moments [J]. Engineering Structures, 2020,219:110755-110770.
25. Chen Q-J, Lei J, Bradford M A, et al. Experimental study on seismic performance of spatial and planar hoop-head mortise and tenon timber joints in historical architecture [J]. Construction and Building Materials, 2024,438:136989-137008.
26. Zhang B, Song X, Xie Q, et al. Seismic behavior of looseness-induced inclined mortise and tenon joints in ancient timber structures: Experimental tests, multi-scale finite element model, and behavior degradation [J]. Engineering Structures, 2024, 318.
27. Lu W, Qiu H, Bu W, et al. Effects of environmental humidity on the gap of mortise-tenon joints: Experimental and numerical investigations [J]. Structures, 2024, 64: 106609-106622.Cui B, Wang C, Wang Y, et al. In-situ growth of scaly carbon nanotube by Cu@Ni core-shell catalyst on continuous carbon fiber surface for multiply tenoned composite interphase [J]. Composites Communications, 2023, 42.
28. Wang H, You J, Tian Y, et al. Digital composite lattice materials for fast but robust assembly [J]. Materials Letters, 2024, 376.
29. Qin Y, Xiong C, Zhu X, et al. Strength analysis of carbon-fiber dovetail tenon connections under quasi-static tension [J]. Structures, 2024, 67: 106925-106939.
30. Aqel R, Severson P, Elhajjar R. A dovetail core design for joints in composite sandwich structures [J]. Composite Structures, 2024, 327: 117700-117707.
31. Lin Q, Zhu X, Yuan J, et al. A hybridized continuum-discontinuum modeling for investigating the fracture and energy evolution characteristics of rock mass under sequential explosive detonation using a bilinear cohesive fracture model [J]. Computers and Geotechnics, 2023,162: 105607-105626.
32. Hu L B, Cong Y, Xia Z X, et al. Recoverability degradation of adhesion between soft matters under uniaxial cyclic bonding–debonding: Modified cohesive interface model and numerical implementation [J]. Engineering Fracture Mechanics, 2024, 310: 110444-110461.